The Influence of Pre-Existing Rib Fractures on GHBMC Thorax Response in Lateral Impact

Lauren Wood Zaseck, Cong Chen, Jingwen Hu, Matthew P. Reed, Jonathan D. Rupp

Abstract: Post-mortem human subjects with pre-existing rib fractures are typically excluded from impact studies with the assumption that the fractures will alter thoracic response to loading. Given that the number of pre-existing rib fractures required to alter thorax response is unknown, this study aimed to use the Global Human Body Models Consortium 50th percentile whole-body finite element model to explore the influence of pre-existing fractures on thorax response to lateral loading. Up to six pre-existing fractures were simulated on the anterior or lateral rib regions, and the model was subjected to a flat-wall, lateral impact at initial speeds of 6.7 m/s or 8.9 m/s. Models with up to three pre-existing fractures on the impacted and/or unimpacted ribs had similar thoracic response as the baseline model with no pre-existing fractures. Conversely, models with pre-existing fractures on ribs 2-7 of either the impacted or unimpacted ribcage exhibited changes in kinematics, increased rib strains, and/or decreases in chest deformations. The observed changes, however, were small relative to mid-size male target response corridors for the loading condition simulated. The results therefore suggest that post-mortem human subjects with pre-existing fractures on up to three ribs may be appropriate for use in lateral impact testing.

Keywords finite-element modelling, lateral impact, rib fracture, thoracic response

I. INTRODUCTION

The field of impact biomechanics relies heavily on the use of post mortem human subjects (PMHS) to establish the biomechanical response and injury tolerance of live humans to impact [1]. PMHS must pass strict inclusion criteria for use in impact testing, which may include specifications for age, weight, bone mineral density, and skeletal structural integrity. As a result, many PMHS that are considered for biomechanical impact testing are ultimately excluded.

One of the major obstacles in obtaining adequate PMHS for impact studies is the presence of pre-existing rib fractures (PERFs). Many PMHS that are considered for biomechanical impact testing are elderly persons who had undergone cardiopulmonary resuscitation (CPR), which frequently results in multiple fractured ribs [2]. Additionally, those PMHS without identified fractures chosen for use typically undergo only one impact test over concerns that any resulting rib fractures will influence the results of subsequent testing. When multiple tests are conducted on a single subject, the impacts are typically designed to be substantially below the threshold for skeletal injury [3-5]. However, any results from subsequent tests are usually interpreted with caution since the influence of the first test on response is unknown, even if no injuries were apparent. The effects of the number and location of PERFs on thorax response and tolerance is currently unknown, but it is likely that thorax response is dependent on the location of any PERF relative to the location and direction of loading.

Physical testing with cadavers cannot reasonably be used to study this problem as no two cadavers are identical and thus comparisons of the responses of subjects with and without PERFs are confounded with intersubject variability. However, simulations with a well-validated whole body finite element model, and the associated deterministic outcome, allow the effects of PERFs, along with comparisons of local rib-level stresses and strains, to be studied. Therefore, this study used the Global Human Body Models Consortium 50th percentile male (GHBMC M50-O)[6] whole body finite element (FE) model to explore the influence of PERFs on thorax response to pure lateral loading.

II. METHODS

GHBMC Finite Element Model

L.W. Zaseck (laurekat@umich.edu; 734-615-3408) is an Assistant Research Scientist, C. Chen is an Engineer in Research, J. Hu is an Associate Research Scientist, M. Reed is a Research Professor, and J. Rupp is a Research Associate Professor at the University of Michigan Transportation Research Institute, Michigan, USA.

The GHBMC M50-O FE model was used in this study. Model geometry was based on medical images of a 26-year-old male [6]. The size of elements in the ribs was 2.5 mm X 2.5 mm on average. Rib material properties and failure criteria were the default GHBMC values. Specifically, ribs were modelled as an elastic-plastic material with plastic failure defined at 1.8% and 13% plastic strain for the cortical and trabecular components, respectively. These properties represent a 50-year-old occupant [7]. To simulate the occurrence of rib fractures, elements were deleted when they reached their plastic failure threshold.

Modeling of Pre-Existing Rib Fractures

PERFs were simulated by detaching elements through the cross-section of both the 2D shell (cortical bone) and 3D solid (cancellous bone) elements of the rib. Contacts were added to the detached surfaces using *CONTACT_AUTOMATIC_SURFACE_TO_SURFACE in LS-DYNA. Friction at the fracture interface was set at 0.3. PERFs were simulated on either the anterior region of the rib approximately 20 mm lateral to the costochondral joint (CCJ), or on the lateral region of the rib, approximately 40-50% along the length of the rib, as measured from the CCJ. These locations correspond to the rib regions most commonly fractured during CPR [10] (Fig. 1).

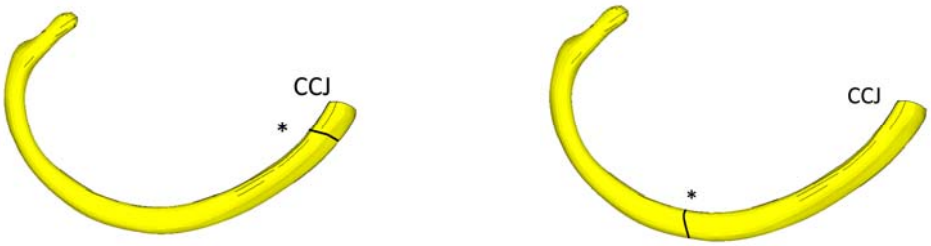

Fig. 1. Location of simulated PERFs (indicated with *) located on the anterior rib (left), or lateral rib (right) regions. Anterior PERFs were located approximately 20mm lateral to the costrochondral joint (CCJ), and lateral PERFs were located at the lateral rib region (approximately 40-50% along the length of the rib).

Simulation Setup and Matrix

The test set-up simulated the [8] tests used for GHBMC model validation [9], with the human model impacting a flat, segmented load wall (Fig. 2). The load wall segments were modelled as rigid bodies. The model was settled onto the flat, rigid seat under gravity for 100 ms. The interface between the model and the seat was frictionless. The model was then accelerated into the load wall so that the left side of the model contacted the wall. This was achieved by setting an initial speed of either 6.7 m/s or 8.9 m/s to all nodes in the model. Simulations were run using LS-DYNA (Livermore Software Technology Corporation, Livermore, CA) MMP971 R6.1.0 with 40 processors on the University of Michigan's Advanced Research Computing cluster (Flux).

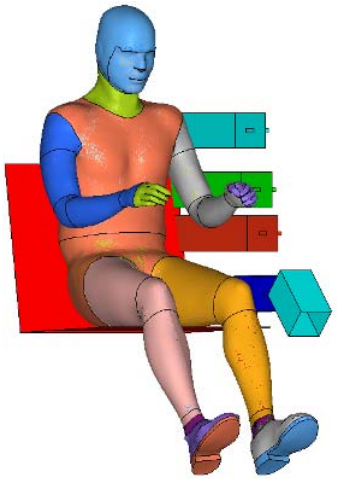

Fig. 2. Set up for the model used in this study, which simulates the [8] Heidelberg-type sled tests, with the model impacting the load wall at initial velocities of 6.7- or 8.9-m/s.

The conditions simulated are shown in Table 1. The simulations with PERFs included fractures on one or six ribs, which is representative of the range of fractures typically sustained during CPR [2][10]. In total, 32

simulations were conducted. For each velocity condition, twelve simulations were conducted with a single PERF. These included models with a PERF on ribs two, four, or six on the impacted (left) or unimpacted (right) ribs. The fractures were located on either the anterior or lateral rib regions. Additionally, for each velocity condition, six simulations were conducted with six PERFs. These included four models with PERFs on ribs 2-7 on either the impacted or unimpacted ribs, and two models with bilateral PERFs on ribs 3-5, with fractures located on either the anterior or lateral rib regions. All simulations were compared with a baseline model with no PERFs. Simulations are designated by their model velocity, fracture location, and fracture region (i.e., *8.9_R4_Lat* refers to the model with an initial velocity of 8.9 m/s and a PERF on the lateral region of right rib 4). Baseline models are designated by their model velocity and *Base* (i.e., *6.7_Base*).

TABLE I
CONDITIONS SIMULATED

Initial Model Speed (m/s)	*Pre-Existing Rib Fracture Location*	*Rib Region for Pre-Existing Fractures*
6.7 or 8.9	Right rib 2, 4, or 6 Left rib 2, 4, or 6 Right ribs 2-7 Left ribs 2-7 Right ribs 3-5 and left ribs 3-5	Anterior or lateral

Data Extraction and Processing

All simulation data were extracted using LS-PrePost 4.3 (Livermore Software Technology Corporation, Livermore, CA). Rib fracture location was defined along the outside of each rib with the origin (0%) at the costovertebral joint (CVJ) and the termination (100%) at the costochondral joint (CCJ). The time of each fracture was also obtained from the simulation data, with t=0 defined at the onset of initial model contact with the load wall. Applied force data were extracted from the model load wall at the shoulder, thorax, and abdomen. Raw force data were filtered with SAE class 180 filtering. Maximum plastic strain was also examined for all rib elements.

External half-thorax deformations were determined using the built-in GHBMC upper and middle chestbands, which pass over the sternum at the level of rib 4 and 6, respectively. A reference line was defined as the line between the most posterior node at the spine and the node passing over the sternum on each chestband. Initial external half-thorax width was determined as the perpendicular distance between the most lateral point of the chestband on the impacted side and the reference line (Fig. 3). External half-thorax deformations were calculated as the percent change of length in this perpendicular line at each time point during the simulation.

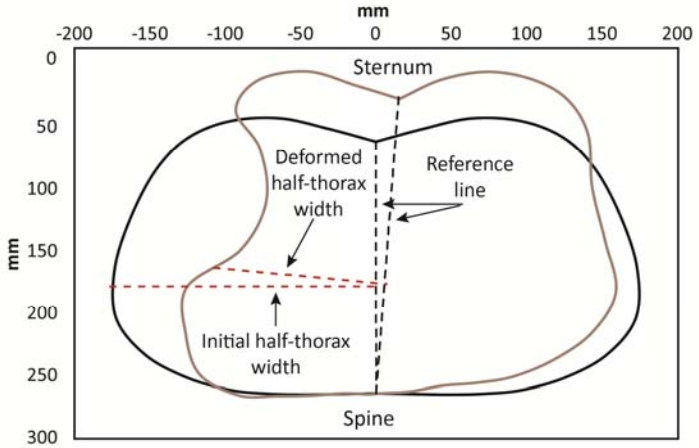

Fig. 3. Illustration of half-thorax calculation for both the initial and deformed chestband contours.

III. RESULTS

Kinematics

Representative model kinematics for the 6.7 m/s and 8.9 m/s conditions are shown in Fig. 4 and Fig. 5, respectively. For the 6.7 m/s condition, the majority of simulations showed kinematics similar to the baseline condition, with full shoulder, arm, and leg contact on their respective load cells, and head contact on the top of the shoulder load cell (Fig. 4, dark grey). The simulation with PERFs on the lateral region of ribs 2-7 on the unimpacted side (*6.7_R2-7_Lat*) exhibited kinematics different from that of the baseline model, with no head contact and the torso slightly angled away from the load cell (Fig. 4, light grey).

For the 8.9 m/s condition, the majority of simulations also showed kinematics similar to the baseline condition. This included more extremity flail than was seen in the 6.7 m/s condition; full shoulder, arm, and leg contact on their respective load cells; and head contact on the shoulder load cell (Fig. 5, dark grey). Two simulations with PERFs on ribs 2-7 (*8.9_L2-7_Ant* and *8.9_R2-7_Lat*) exhibited different kinematics from baseline, with no head contact and the torso slightly angled away from the load wall (Fig. 5, light grey).

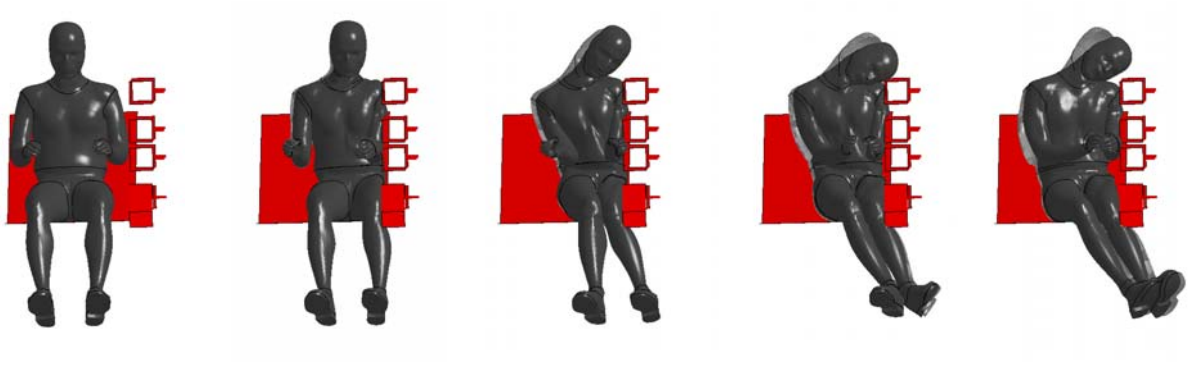

0ms 20ms 40ms 60ms 80ms

Fig. 4. Representative model kinematics for the 6.7 m/s condition. The dark grey represents model kinematics observed in the majority of simulations, including the baseline condition with no PERFs. The light grey shows the kinematics from model *6.7_R2-7_Lat*, which exhibited variations in head and torso kinematics.

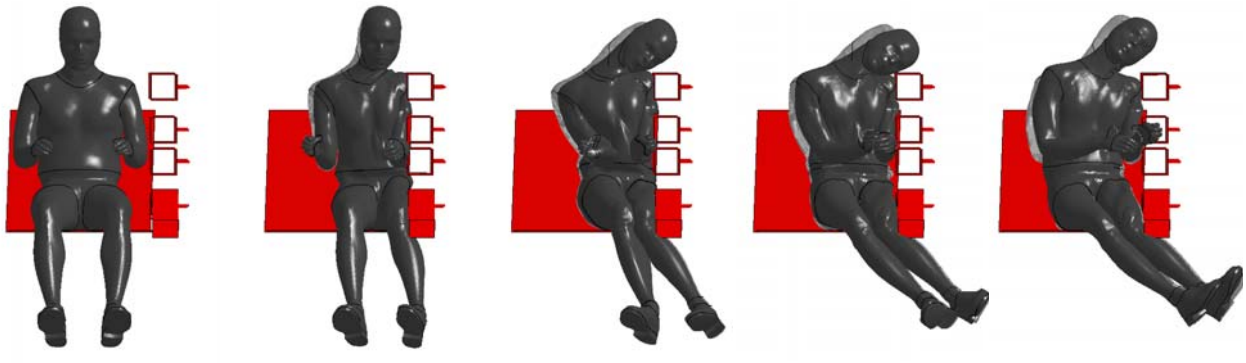

0ms 20ms 40ms 60ms 80ms

Fig. 5. Representative model kinematics for the 8.9 m/s condition. The dark grey represents model kinematics observed in the majority of simulations, including the baseline condition. The light grey shows kinematics from the models that exhibited variations in head and torso kinematics (*8.9_L2-7_Ant* and *8.9_R2-7_Lat*).

Fracture Prediction

For the 6.7 m/s condition, the baseline model predicted four fractured ribs, all on the impacted side (left ribs 4-7). For the 8.9 m/s condition, the baseline model predicted seven fractured ribs, all on the impacted side (left ribs 2-8). The presence of PERFs did not result in any additional fractures on ribs not fractured in the baseline models. In most cases, no additional fractures were predicted during the simulation on a rib with a PERF. The

timing and location of all predicted fractures remained largely unchanged in the 6.7 m/s and 8.9 m/s simulations. The one exception occurred with the predicted fracture on left rib 7. In the majority of the 6.7 and 8.9 m/s models, including the baseline models, a fracture on left rib 7 was predicted at a location of 64% along the rib. In approximately a third of the models, the fracture occurred more anterior on the rib, at a location of 83% along the rib. No obvious trend was observed with respect to which simulations predicted the altered fracture location of rib 7. See Appendix Tables AI and AII for predicted rib fracture information for all simulations.

Applied Forces

PERFs on the anterior region of the rib had no influence on applied shoulder, thorax, or abdomen force histories in any of the 6.7 m/s (Fig. 6) or 8.9 m/s (Fig. 7) simulations. In both the 6.7 m/s and 8.9 m/s simulations with PERFs in the lateral region of right ribs 2-7, maximum applied shoulder force was 34% and 30%, respectively, above that seen in their respective baseline models. This was accompanied by a decrease in maximum applied thorax force in both models of approximately 15% compared to baseline. Maximum applied forces to the abdomen increased approximately 25% in four simulations (*8.9_R2_Lat, 8.9_R4_Lat, 8.9_L4_Lat, 8.9_R3-5L3-5_Lat*). Maximum applied forces and deformations are shown in the Appendix, Table AIII for all simulations.

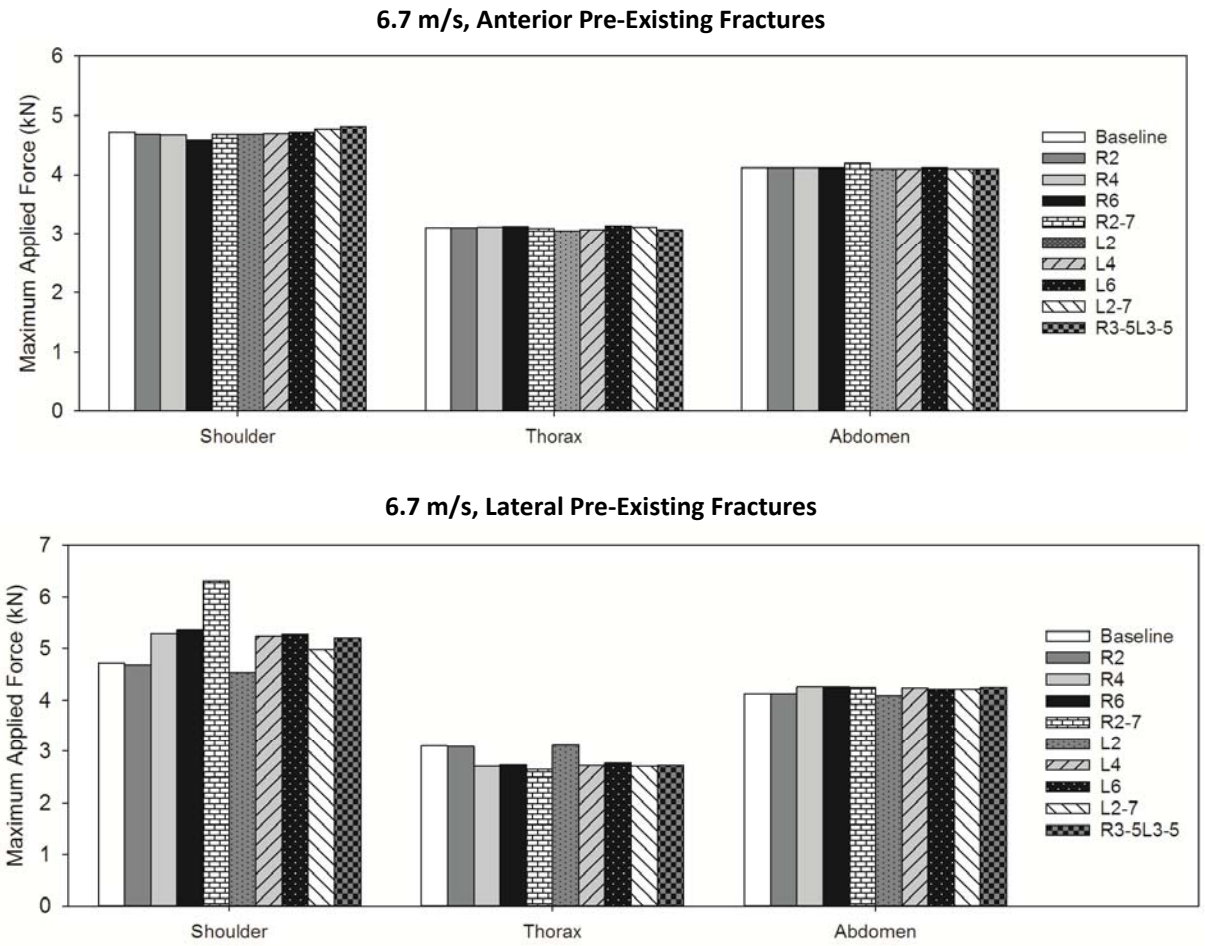

Fig. 6. Maximum applied forces for the shoulder, thorax, and abdomen in the 6.7 m/s impact condition for anterior (top) and lateral (bottom) pre-existing fractures.

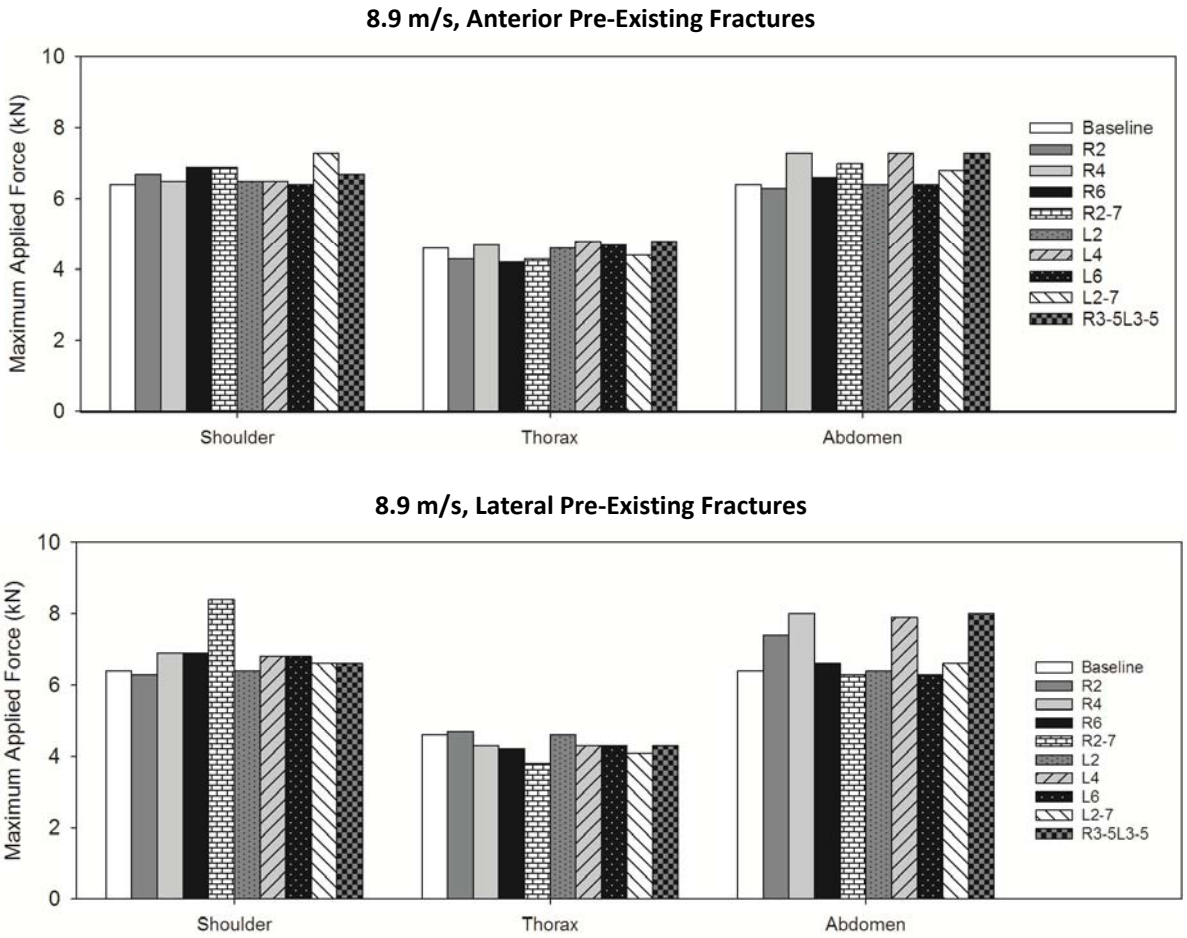

Fig. 7. Maximum applied forces for the shoulder, thorax, and abdomen in the 8.9 m/s impact condition for anterior (top) and lateral (bottom) pre-existing fractures.

Force-Deformation Responses

Representative upper chestband contours at maximum half-thorax deformation are shown in Fig. 8. Half-thorax force-deformation responses for the external upper and middle thorax are shown in Fig. 9 and Fig. 10 for 6.7 m/s and 8.9 m/s, respectively. PERFs on the anterior rib portion had little influence on the force-deformation response of all simulations. With the exception of *6.7_L2_Lat* and *8.9_L2_Lat*, all models with PERFs on the lateral rib portion had maximum thorax compressions and applied forces lower than baseline with the greatest changes occurring in models with the PERFs on right ribs 2-7. Force-deformation responses for all simulations are shown in the Appendix, Tables AIV and AV.

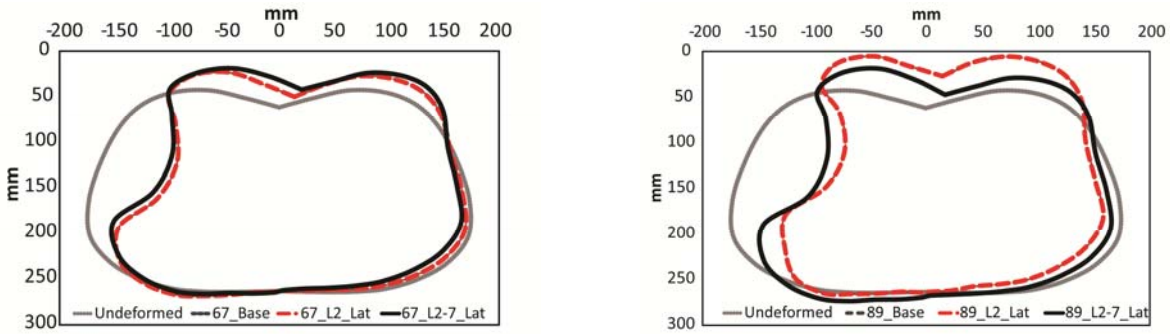

Fig. 8. Representative chestband contours at maximum half-thorax deformation for 6.7 m/s (left) and 8.9 m/s (right) simulations.

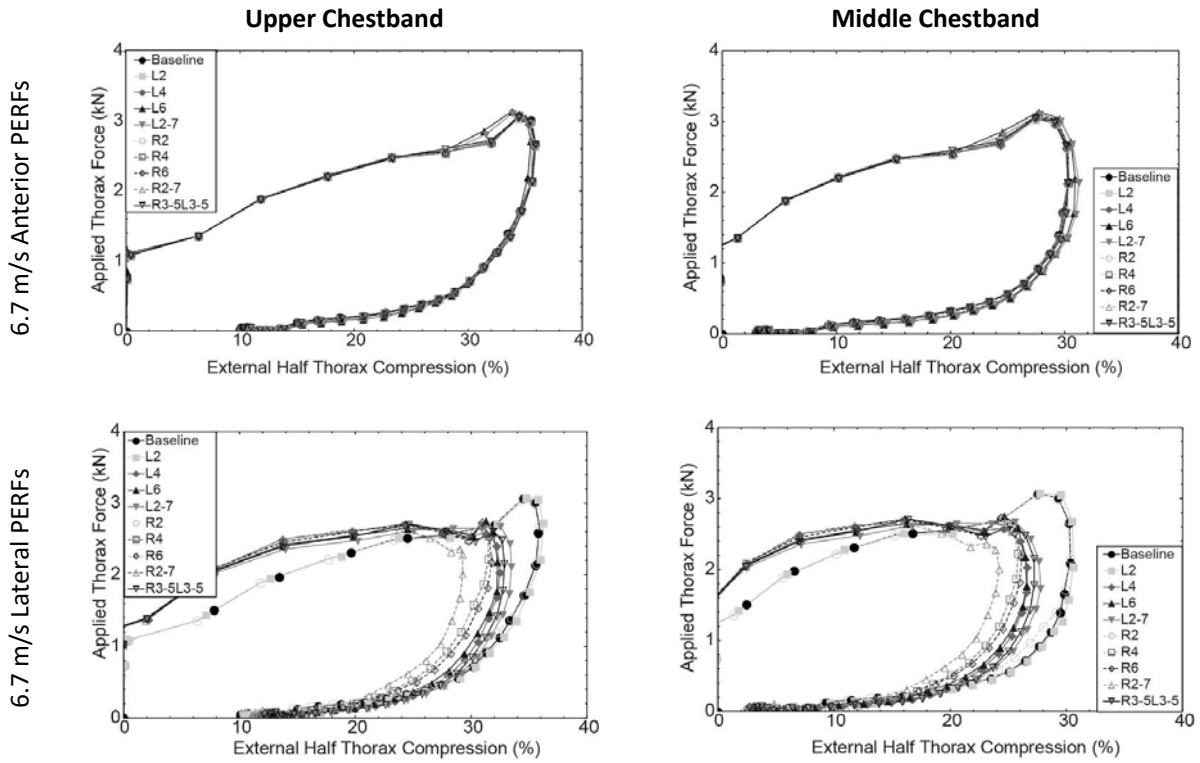

Fig. 9. Thorax force-deformation plots for the 6.7 m/s condition with pre-existing fractures on the anterior rib portion (top row) and the lateral rib portion (bottom row).

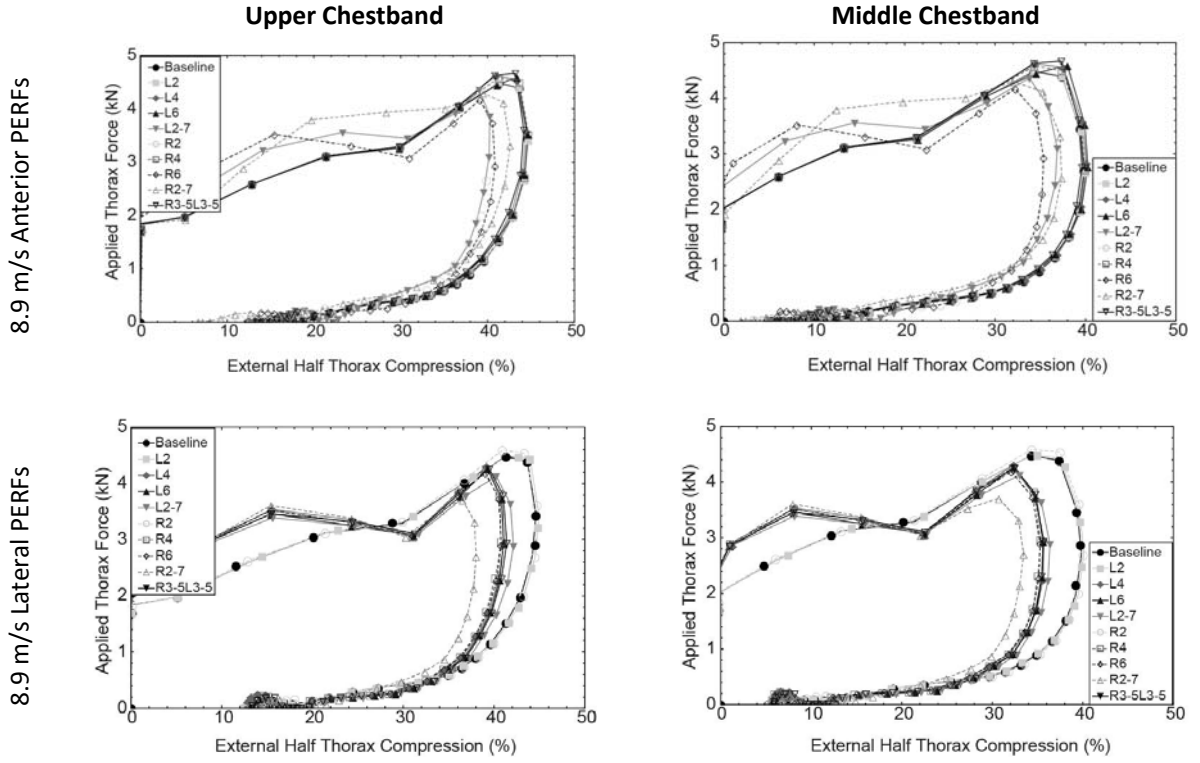

Fig. 10. Thorax force-deformation plots for the 8.9 m/s condition with pre-existing fractures on the anterior rib portion (top row) and the lateral rib portion (bottom row).

Rib Plastic Strain

Example maximum plastic strain distributions are shown in Figs. 11 and 12 for the 6.7 m/s and 8.7 m/s impact conditions, respectively. Compared to baseline, for both impact speeds, PERFs on the impacted side tended to reduce the plastic strain along any rib that was pre-fractured. PERFs on the unimpacted side tended to have little effect on plastic strain concentrations on the impacted side. The two exceptions were the two models with PERFs on the lateral region of unimpacted ribs 2-7 (*6.7_R2-7_Lat* and *8.9_R2-7_Lat*), which saw an increase in plastic strain on impacted ribs 8 and 9 caused by left elbow contact with the ribcage. Plastic strains were low on the unimpacted ribs in all cases, aside for the anterior regions of ribs 7-10, which correspond to the location where the model's right elbow contacted the thorax.

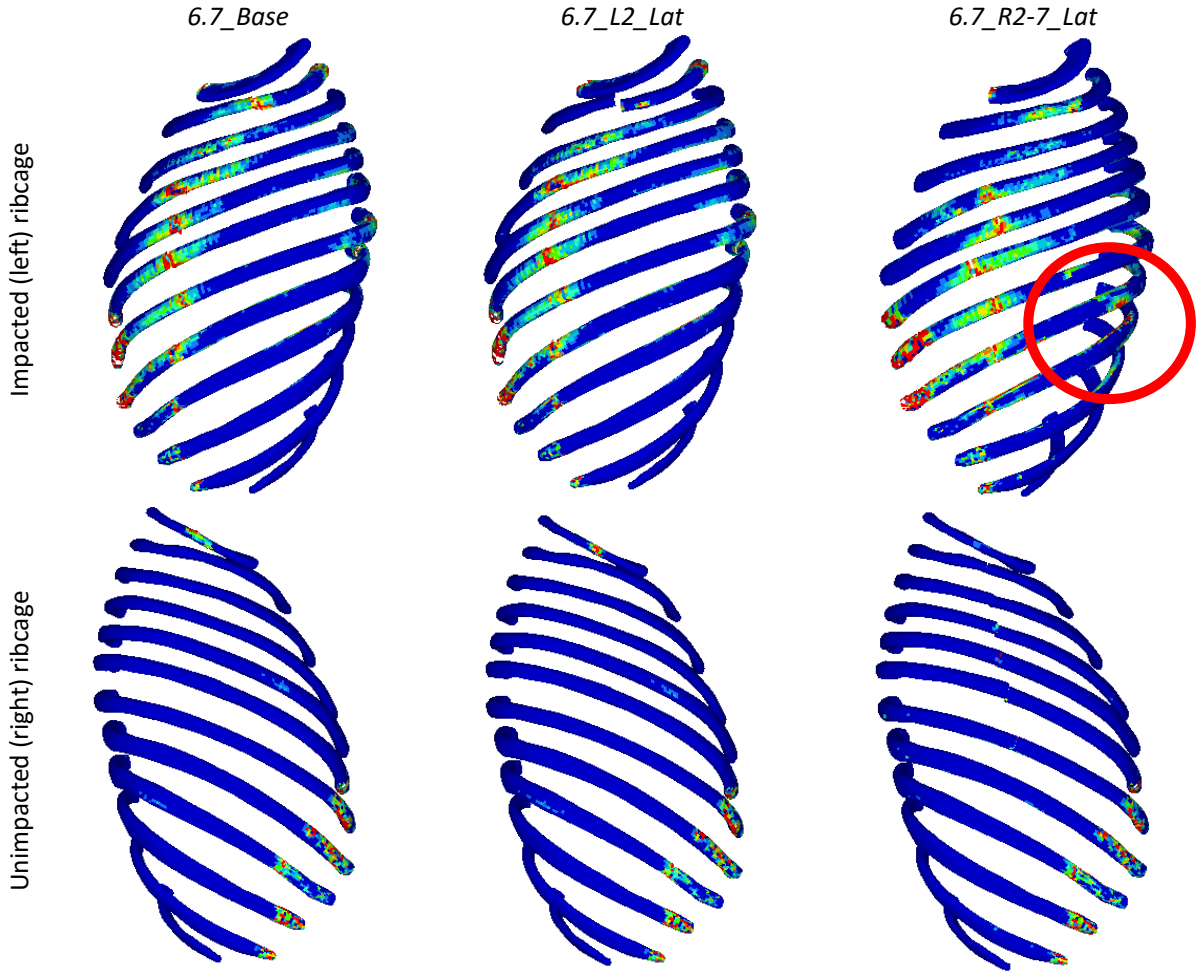

Fig. 11. Example maximum plastic strains for the 6.7 m/s impact conditions. The baseline response is shown in the left column. The majority of simulations had a strain response (e.g., middle column) similar to that seen in the baseline model. The model with PERFs on the lateral region of right ribs 2-7 showed increased strains on left ribs 8 and 9 (right column). Blue and red indicate 0% and 1.8% plastic strain, respectively.

8.9_Base *8.9_R4_Ant* *8.9_R2-7_Lat*

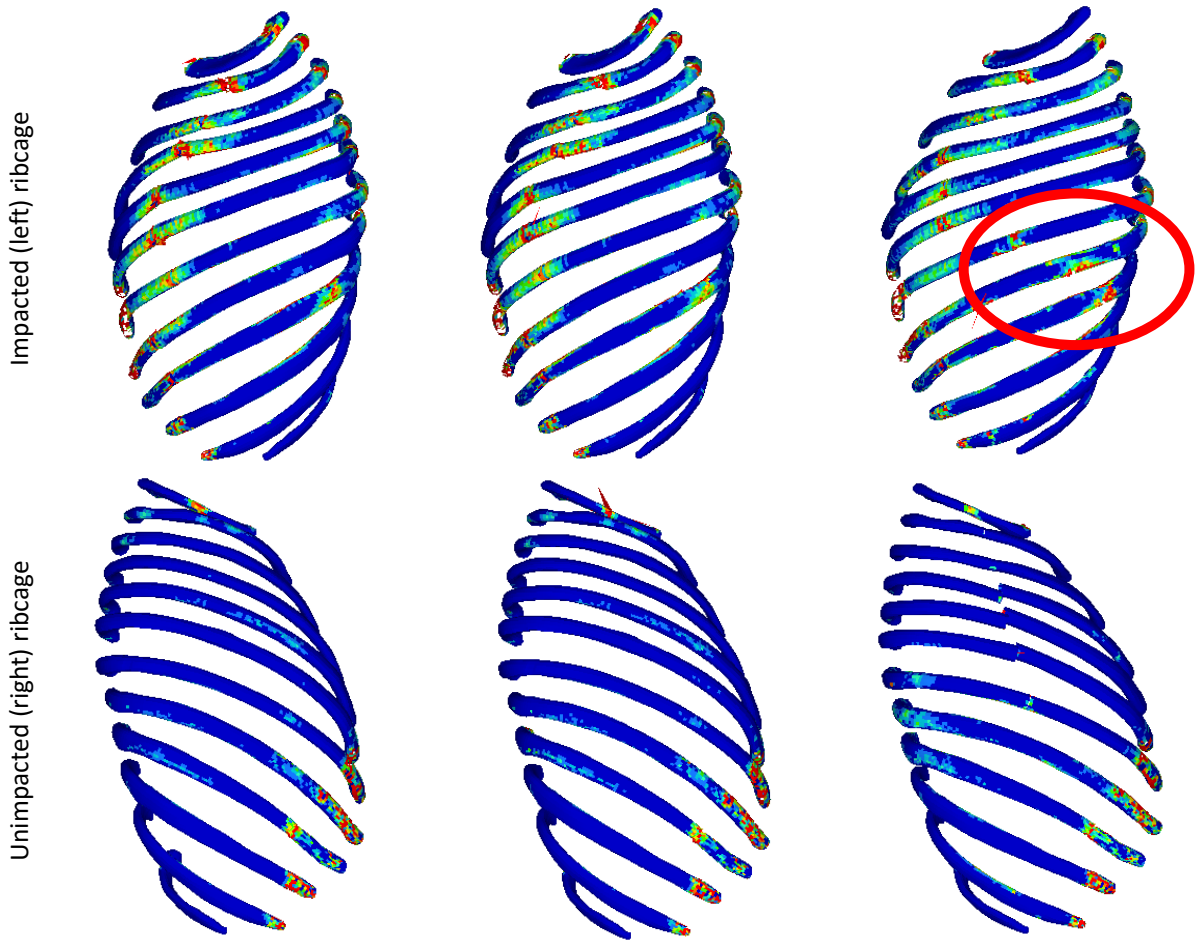

Fig. 12. Example maximum plastic strains for the 8.9-m/s impact condition. The baseline response is shown in the left column. The majority of simulations had a strain response similar to that seen in the baseline model (e.g., middle column). The model with PERFs on the lateral region of right ribs 2-7 showed increased strains on left ribs 8 and 9 (right column). Blue and red indicate 0% and 1.8% plastic strain, respectively.

IV. DISCUSSION

This study examined the influence of PERFs on the GHBMC thorax response in moderate and high-speed lateral loading. The results suggest that PERFs can influence thorax response in lateral loading, and the effect of PERFs depends on their location and number. Specifically, local rib instability caused by up to three fractured ribs in the superior half of the ribcage was compensated for by the surrounding ribcage structure. That is, the baseline GHBMC thorax response is unchanged when there is either a single PERF on the superior half of the ribcage, or up to three bilateral fractures on ribs 3-5. This finding was unaffected by the location of the PERF relative to the point of impact.

Results of previous studies with PMHS support the finding that a small number of rib fractures does not influence thorax response. Quasi-static impact tests on eviscerated PMHS thoraces demonstrated that the repeatability of a subject that experienced rib fracture during the first loading event was comparable to the repeatability of a different subject that did not experience rib fracture [11]. Previous studies involving lateral pendulum impacts [12], anterior pendulum impacts [13], and frontal belt loading [14] of PMHS have also noted that thoracic injuries with a wide range of severity can occur with no appreciable changes in impact forces. This may be explained by redundant load sharing among the upper ribs [11][13], which is an observation supported by the present study. Patterns of plastic strain in the ribcage (Figs. 11 and 12) show that the majority of the load was transferred through the impacted side ribs, even when there were six PERFs on the impacted side. Plastic strain remained low on all unimpacted ribs, except in locations where the model's right arm contacted the thorax. Similar strain patterns of struck-side and unimpacted ribs have been observed in PMHS thoraces

undergoing lateral ram impacts [15].

For both initial impact velocities, the greatest changes in model kinematic response occurred when PERFs were located on the lateral region of ribs 2-7 on either the impacted or unimpacted side. In these models, the simulation predicted slight thorax rotation away from the load wall that was not seen in the baseline models. Pelvis kinematics were no different in these models than in the baseline models. Since kinematics of the models with six PERFs on the anterior rib region were similar to the baseline model response, the influence of a large number of PERFs on kinematics appears to be dependent on the location of the fractures with respect to the location of the loading.

In the models with six PERFs on the lateral rib region, ribcage kinematics show that the separated segments of ribs with PERFs moved independently during the initial acceleration of the model. This resulted in an anterior bowing of the sternum and altered rib displacement compared to the baseline models (Fig. 13). These differences in ribcage kinematics may explain the slight reduction in half-thorax compression seen in models with six PERFs (*6.7_R2-7_Lat* and *8.9_R2-7_Lat*) compared to baseline.

The results indicate that arm posture has the potential to influence local rib strain response. Although no additional rib fractures were predicted in the *R2-7_Lat* models compared to the baseline, higher plastic strain on ribs 8 and 9 was predicted on the struck side that were not predicted in the baseline models. These strain concentrations are located near the left humerus and elbow of the model. Increased occurrence of rib fractures in the GHBMC thorax directly under the model's humerus has also been observed [9]. Coupled with the present study, the results suggest that arm posture can have a significant influence on the loading patterns of ribs.

One potential limitation of this work is the use of element deletion to simulate rib fracture. In the present study, the ribs were modelled as a piecewise linear plastic material with element deletion once a plastic strain of 1.8% or 13% in the cortical or trabecular bone, respectively, was reached. The failure behavior of elements in the rib, however, will be dependent on the value selected for ultimate plastic strain. For example, a lower value for ultimate plastic strain, as could be expected in ribcages from elderly persons, would likely result in a greater number of fractured ribs. The size of elements in the model can also influence the local strain response. Additionally, by using plastic strain as the model output, no information is learned about the strain profiles that did not reach plastic strain. As an alternative, true strain for every element could be determined without deletion of any elements. However, since changes in local ribcage geometry and load sharing due to rib fractures are not accounted for if element deletion is not used, rib fracture was induced in the present study.

The results presented are representative of pure lateral impacts using a flat wall with contact to the shoulder, thorax, abdomen, and pelvis. It is likely that any change in impactor geometry will change the manner in which PERFs influence thorax response. Flat wall lateral impacts that do not engage the shoulder produce model kinematics that vary substantially from those that do engage the shoulder [9]. Likewise, load walls with offsets produce focal loading and different injury patterns than flat load walls [16-17]. It is therefore likely that the location and number of PERFs that lead to an altered thorax response in pure lateral loading may change based

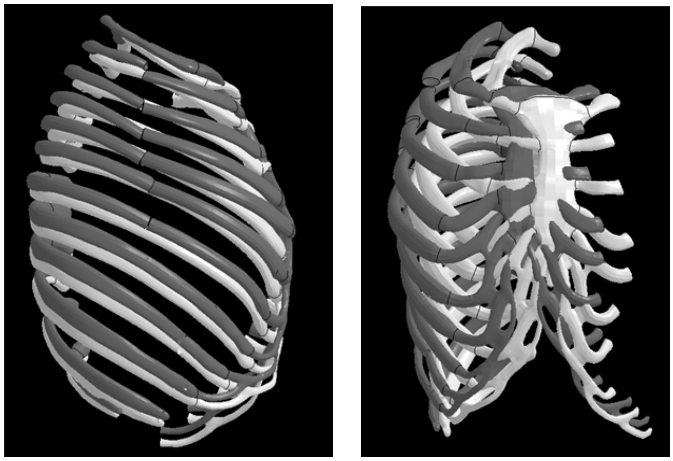

Fig. 13. Lateral (left) and anterior (right) views of the right ribcage, coastal cartilage, and sternum in the 8.9_Base model (white) and 8.9_R2-7_Lat model (grey). Images taken at t = 20 ms.

on impactor size and shape. Oblique or frontal loading engages the ribcage differently than lateral loading, and

it has been shown that thorax response to pure lateral loading differs from that seen in oblique lateral loading [5]. Therefore, the location and number of PERFs important in altering thorax response to loading will also likely be influenced by the direction of the loading.

An interesting observation of the present study was that the magnitude of chest deformation was highly dependent on whether the deformations were calculated as a function of half or full-thorax width. PERFs resulted in independent movement of individual ribs during the loading event, and the effect became more pronounced as the number of PERFs increased. Chest deformations based on full-thorax width were therefore a less useful measure of the true deformation of the ribcage than chest deformations based on half-thorax width.

Finally, the present investigation used FE models with a single ribcage geometry and constant rib material properties. The ribcage geometry of the GHBMC M50-O model was created from the scans of a younger, living person while the material properties of the ribs were derived from older, deceased persons. Not only do rib material properties change with aging [18], but so does rib angle [19] and cortical thickness [20]. Ribcage cartilage also becomes calcified and brittle with aging [21], likely influencing the mechanical response of the thorax. Overall thorax response in PMHS is also highly dependent on the surrounding superficial tissues and viscera [3]. The choice of rib geometry and material properties in FE models has been shown to influence both local rib fracture characteristics [22] and strain response [23], as well as overall thorax response [24]. Therefore, the results presented here likely do not represent the response of the younger body shape and geometry that the model was developed from. However, the goal of this investigation was to determine relative differences among models while keeping material properties and geometry, aside from the induced fractures, constant. Given that ribcage geometry cannot be completely predicted by sex, age, and body size [25] the influence of material properties on thorax response using age and subject-specific FE models is an important avenue for future investigation.

Despite limitations, the present study provides important data regarding the influence of PERFs on thoracic response that could not have been obtained with physical testing of PMHS. The GHBMC full-body FE model allows for the direct examination of the influence of PERFs while keeping all other factors constant. Conversely, the large intersubject variation in PMHS physical and material properties precludes direct relationships from being made between thoracic response and the number and location of PERFs. This study shows that up to three PERFs on the struck and/or unimpacted-side ribcage do not result in changes in either the local rib mechanical response or the overall thoracic response to flat-wall lateral loading. Therefore, PMHS with up to three PERFs on each side of the ribcage may be appropriate for use in impact testing using the examined loading condition. Future modelling efforts using subject-specific rib geometries and material properties will be valuable to further elucidate the influence of PERFs in a wide range of occupant populations.

V. CONCLUSIONS

This study examined the influence of PERFs on the GHBMC thorax response in lateral impact. The simulations demonstrate that any local changes in rib response induced by a single rib fracture did not result in changes in overall thoracic response. Bilateral PERFs on ribs 3-5 also did not influence overall thoracic response. Changes in model kinematics, local rib strains, and force-deformation responses were seen in models with six PERFs on the unimpacted ribcage. The observed changes, however, were small relative to mid-size male target response corridors for the loading condition simulated. The influence of PERFs on thorax response appears to be dependent on both the number and location of the fractures with respect to the direction of the loading. Therefore, PMHS with a small number of PERFs may be appropriate for use in flat wall lateral impact testing.

VI. REFERENCES

[1] Crandall J, Bose D, *et al*. (2011) Human surrogates for injury biomechanics research. Clinical Anatomy,**24**(3): pp.362–371.

[2] Hoke RS, Chamberlain D. (2004) Skeletal chest injuries secondary to cardiopulmonary resuscitation. Resuscitation,,**63**: pp.327–338.

[3] Kent R. (2008) Frontal thoracic response to dynamic loading: the role of superficial tissues, viscera and the rib cage. International Journal of Crashworthiness,**13**(3): pp.289–300.

[4] Kent R, Lessley D, and Sherwood C. (2004) Thoracic response to dynamic, non-impact loading from a hub, distributed belt, diagonal belt, and double diagonal belt. Stapp Car Crash Journal,**48**: pp.495–519.

[5] Shaw JM, Herriott RG, McFadden JD, Donnelly BR, Bolte JH. (2006) Oblique and lateral impact response of

the PMHS thorax. Stapp Car Crash Journal,**50**: pp.147–167.
[6] Gayzik FS, Moreno DP, Vavalle NA, Rhyne AC, Stitzel JD. (2011) Development of the Global Human Body Models Consortium mid-sized male full body model. Injury Biomechanics Research Workshop, 2011.
[7] Golman AJ, Danelson KA, Miller LE, Stitzel JD. (2014) Injury prediction in a side impact crash using human body model simulation. Accident Analysis and Prevention,**64**: pp.1–8.
[8] Cavanaugh JM, Walilko TJ, Malhotra A, Zhu Y, King AI. (1990) Biomechanical response and injury tolerance of the pelvis in twelve sled side impacts. SAE Technical Paper No. 902305.
[9] Vavalle NA, Moreno DP, Rhyne AC, Stitzel JD, Gayzik FS. (2012) Lateral impact validation of a geometrically accurate full body finite element model for blunt injury prevention. *Annals of Biomedical Engineering*,**41**(3): pp.497–512.
[10] Pinto DC, Haden-Pinneri K, Love JC. (2013) Manual and automated cardiopulmonary resuscitation (CPR): a comparison of associated injury patterns. Journal of Forensic Science,**58**(4): pp.904–909.
[11] Kindig MW, Lau AG, Forman JL, Kent RW. (2010) Structural response of cadaveric ribcages under a localized loading: stiffness and kinematic trends. Stapp Car Crash Journal,**54**: pp.337–380.
[12] Yoganandan N, Pintar FA, Gennarelli T. (2004) Small female-specific biomechanical corridors in side impact. Proceedings of the IRCOBI Conference, 2004, Graz Austria.
[13] Shaw G, Lessley D, *et al*. (2007) Quasi-static and dynamic thoracic loading tests: cadaveric torsos. Proceedings of the IRCOBI Conference, 2007, Maastricht, The Netherlands.
[14] Duma S, Stitzel J, Kemper A, McNally C, Kennedy E, Matsuoka F. (2006) Non-censored rib fracture data from dynamic belt loading tests on the human cadaver thorax. Biomedical Sciences Instrumentation, **42**: pp.148–153.
[15] Trosseille X, Baudrit P, Leport T, Vallancien G. (2008) Rib cage strain pattern as a function of chest loading configuration. Stapp Car Crash Journal, **52**: pp.205–231.
[16] Kuppa S, Eppinger RH, McCoy F, Nguyen T, Pintar FA, Yoganandan N. (2003) Development of side impact thoracic injury criteria and their application to the modified ES-2 dummy with rib extensions (ES-2re). Stapp Car Crash Journal,**47**: pp.289–320.
[17] Maltese M, Eppinger R, Rhule H, Donnelly B, Pintar F, Yoganandan N. (2002) Response targets of human surrogates in lateral impacts. Stapp Car Crash Journal,46: p.321–351.
[18] Agnew AM, Schafman M, Moorhouse K, White SE, Kang YS. (2015) The effect of age on the structural properties of human ribs. Journal of the Mechanical Behavior of Biomedical Materials,**41**: pp.302–314.
[19] Kent R, Lee SH, *et al*. (2005) Structural and material changes in the aging thorax and their role in crash protection for older occupants. Stapp Car Crash Journal,**49**: pp.231–249.
[20] Evans F. (1975) Mechanical properties and histology of cortical bone from younger and older men. The Anatomical Record,**185**: pp.1–11.
[21] Teale C, Romaniuk C, Mulley G. (1989) Calcification on chest radiographs: the association with age. Ageing,**18**: pp.333–336.
[22] Li Z, Kindig MW, Subit D, Kent RW. (2010) Influence of mesh density, cortical thickness, and material properties on human rib fracture prediction. Medical Engineering and Physics,**32**(9): pp.998–1008.
[23] Subit D, Kindig M, *et al*. (2011) Prediction of rib cage fracture in computational modeling: effect of rib cortical thickness distribution and intercoastal muscles mechanical properties. Proceedings of the 39th International Workshop on Human Subjects for Biomechanical Research, 2011.
[24] Antona-Makoshi J, Yamamoto Y, *et al*. (2015) Age-dependent factors affecting thoracic response: a finite element study focused on Japanese elderly occupants. Traffic Injury Prevention,**16**: pp.S66–S74.
[25] Shi X, Cao L, Reed MP, Rupp JD, H CN, Hu J. (2015) A statistical human rib cage geometry model accounting for variations by age, sex, stature and body mass index. Journal of Biomechanics,**47**(10): pp.2277–2285.

VII. APPENDIX

TABLE AI
6.7 M/S RIB FRACTURE INFORMATION

Model ID	Predicted Fractured Ribs [Fracture time (ms), Length along abscissa (%)]	Model ID	Predicted Fractured Ribs [Fracture time (ms), Length along abscissa (%)]
67_Base	L4 (22.5, 66.3) L5(17.5, 64.4) L6 (20, 66.8) L7 (20, 64.4)		
67_L2_Ant	L4 (22.5, 66.4) L5(17.5, 64.5) L6 (20, 66.7) L7 (20, 65.1)	**67_L2_Lat**	L4 (22.5, 67.3) L5(17.5, 65.2) L6 (20, 66.8) L7 (20, 83.2)
67_L4_Ant	L5(17.5, 65.0) L6 (20, 66.1) L7 (20, 65.9)	**67_L4_Lat**	L5(115, 65.2) L6 (117.5, 66.7) L7 (22.5, 64.4)
67_L6_Ant	L4(22.5, 69.1) L5 (17.5, 64.5) L7 (22.5, 83.2)	**67_L6_Lat**	L4(22.5, 78.9) L5 (17.5, 63.8) L7 (22.5, 83.2)
67_L2-7_Ant	N/A	**67_L2-7_Lat**	N/A
67_R2_Ant	L4 (22.5, 68.1) L5(17.5, 64.5) L6 (20, 66.6) L7 (20, 65.1)	**67_R2_Lat**	L4 (22.5, 66.3) L5(17.5, 64.4) L6 (20, 66.8) L7 (20, 64.4)
67_R4_Ant	L4 (22.5, 64.7) L5(17.5, 64.6) L6 (20, 66.1) L7 (20, 65.1)	**67_R4_Lat**	L4 (17.5, 66.3) L5(15, 64.4) L6 (17.5, 66.8) L7 (22.5, 64.4)
67_R6_Ant	L4 (22.5, 66.3) L5(17.5, 64.5) L6 (20, 66.2) L7 (20, 65.1)	**67_R6_Lat**	L4 (17.5, 66.3) L5(15, 64.4) L6 (17.5, 66.8) L7 (22.5, 64.4)
67_R2-7_Ant	L4 (22.5, 68.9) L5(17.5, 64.5) L6 (20, 66.9) L7 (20, 65.1)	**67_R2-7_Lat**	L4 (17.5, 66.3) L5(15, 64.4) L6 (20, 66.8) L7 (22.5, 64.4)
67_R3-5L3-5_Ant	L6 (20, 66.9) L7 (20, 64.5)	**67_R3-5L3-5_Lat**	L6 (20, 66.8) L7 (20, 64.4)

TABLE AII

8.9 M/S RIB FRACTURE INFORMATION

Model ID	Predicted Fractured Ribs [Fracture time (ms), Length along abscissa (%)]	Model ID	Predicted Fractured Ribs [Fracture time (ms), Length along abscissa (%)]
89_Base	L2 (20, 43.3) L3 (20, 52.0) L4 (17.5, 57.7) L5 (17.5, 65.7) L6 (17.5, 67.8) L7 (17.5, 87.6) L8 (25, 73.6)		
89_L2_Ant	L3 (20, 52.7) L4 (15, 56.7) L5 (15, 65.7) L6 (15, 68.2) L7 (15, 89.3) L8 (22.5, 78.9)	**89_L2_Lat**	L3 (17.5, 51.2) L4 (15, 67.2) L5 (12.2, 63.8) L6 (15, 65.3) L7 (15, 86.8) L8 (22.5, 78.6)
89_L4_Ant	L2 (17.5, 43.0) L3 (17.5, 52.0) L5 (15, 66.6) L6 (15, 68.1) L7 (20, 86.6) L8 (22.5, 79.0)	**89_L4_Lat**	L2 (15, 43.1) L3 (15, 51.2) L5 (12.5, 63.8) L6 (152.5, 67.8) L7 (15, 87.6) L8 (20, 78.6)
89_L6_Ant	L2 (20, 42.3) L3 (20, 52.5) L4 (17.5, 55.8) L5 (17.5, 64.9) L7 (17.5, 84.4) L8 (25, 78.0)	**89_L6_Lat**	L2 (17.5, 43.1) L3 (15, 51.2) L4 (12.5, 78) L5 (12.5, 63.8) L7 (15, 85.3) L8 (20, 78.6)
89_L2-7_Ant	L8 (17.5, 70.5)	**89_L2-7_Lat**	L8 (17.5, 78.0)
89_R2_Ant	L2 (15, 41.7) L3 (15, 51.7) L4 (15, 64.5) L5 (12.5, 65.1) L6 (15, 66.1) L7 (15, 84.6) L8 (22.5, 73.6)	**89_R2_Lat**	L2 (15, 43.3) L3 (17.5, 52.0) L4 (15, 57.7) L5 (12.5, 65.7) L6 (15, 67.8) L7 (15, 87.6) L8 (22.5, 73.6)
89_R4_Ant	L2 (15, 45.7) L3 (17.5, 52.7) L4 (15, 49.1) L5 (12.5, 66.4) L6 (15, 68.2) L7 (17.5, 87.6) L8 (22.5, 79.0)	**89_R4_Lat**	L2 (12.5, 40.3) L3 (15, 50.9) L4 (12.5, 67.2) L5 (12.5, 63.8) L6 (12.5, 65.3) L7 (15, 86.8) L8 (17.5, 78.6)
89_R6_Ant	L2 (15, 46.2) L3 (17.5, 51.5) L4 (15, 56.6) L5 (12.5, 65.6) L6 (15, 67.8) L7 (17.5, 65.7) L8 (25, 80.7)	**89_R6_Lat**	L2 (12.5, 44.4) L3 (15, 51.2) L4 (12.5, 77.1) L5 (12.5, 63.8) L6 (12.5, 65.3) L7 (15, 84.6) L8 (22.5, 78.6)
89_R2-7_Ant	L2 (15, 41.7) L3 (17.5, 35.5) L4 (15, 68.0) L5 (15, 64.0) L6 (15, 64.7) L7 (17.5, 64.4) L8 (20, 69.1)	**89_R2-7_Lat**	L2 (12.5, 40.3) L3 (15, 50.9) L4 (15, 67.2) L5 (12.5, 63.8) L6 (12.5, 65.3) L7 (17.5, 86.8) L8 (20, 78.6)

89_R3-5L3-5_Ant	L2 (15, 35.1) L6 (15, 59.8) L7 (17.5, 88.3) L8 (22.5, 78.8)

89_R3-5L3-5_Lat	L2 (12.5, 35.1) L6 (15, 59.2) L7 (15, 89.5) L8 (20, 78.6)

TABLE AIII

APPLIED FORCES AND MAXIMUM CHEST DEFORMATIONS

Model ID	Maximum Applied Shoulder Force (kN)	Maximum Applied Thorax Force (kN)	Maximum Applied Abdomen Force (kN)	Maximum Deformation, Upper Chestband (%)	Maximum Deformation, Middle Chestband (%)
67_Base	4.7	3.1	4.1	35.9	30.4
67_L2_Ant	4.7	3.1	4.1	35.9	30.3
67_L2_Lat	4.5	3.1	4.1	36.3	30.6
67_L4_Ant	4.7	3.1	4.1	35.8	30.3
67_L4_Lat	5.2	2.7	4.2	32.5	26.6
67_L6_Ant	4.7	3.1	4.1	35.5	30.9
67_L6_Lat	5.3	2.8	4.2	32.3	26.6
67_L2-7_Ant	4.8	3.1	4.1	35.6	31.2
67_L2-7_Lat	5.0	2.7	4.2	33.5	27.8
67_R2_Ant	4.7	3.1	4.1	35.9	30.4
67_R2_Lat	4.7	3.1	4.1	36.0	30.4
67_R4_Ant	4.7	3.1	4.1	35.9	30.4
67_R4_Lat	4.7	3.1	4.1	31.5	25.8
67_R6_Ant	5.3	2.7	4.3	35.9	30.4
67_R6_Lat	5.4	2.7	4.3	31.8	26.1
67_R2-7_Ant	4.7	3.1	4.2	35.9	30.3
67_R2-7_Lat	6.3	2.7	4.3	29.3	24.2
67_R3-5L3-5_Ant	4.8	3.1	4.1	35.9	30.3
67_R3-5L3-5_Lat	5.2	2.7	4.3	32.9	27.2
89_Base	6.4	4.6	6.4	44.6	39.8
89_L2_Ant	6.5	4.6	6.4	44.7	40.0
89_L2_Lat	6.4	4.6	6.4	45.0	40.1
89_L4_Ant	6.5	4.8	7.3	44.5	40.1
89_L4_Lat	6.8	4.3	7.9	41.1	35.7
89_L6_Ant	6.4	4.7	6.4	44.6	40.3
89_L6_Lat	6.8	4.3	6.3	41.1	35.6
89_L2-7_Ant	7.3	4.4	6.8	40.3	36.9
89_L2-7_Lat	6.6	4.1	6.6	42.1	36.4
89_R2_Ant	6.1	4.5	6.3	39.9	34.5
89_R2_Lat	6.3	4.7	7.4	44.7	40.0
89_R4_Ant	6.5	4.7	7.3	44.7	39.9
89_R4_Lat	6.9	4.3	8	40.8	35.3
89_R6_Ant	6.9	4.2	6.6	40.9	35.4
89_R6_Lat	6.9	4.2	6.6	40.8	35.3
89_R2-7_Ant	6.9	4.3	7	42.6	37.4
89_R2-7_Lat	8.4	3.8	6.3	38.0	33.5
89_R3-5L3-5_Ant	6.7	4.8	7.3	44.2	39.6
89_R3-5L3-5_Lat	6.6	4.3	8	41.4	35.7

TABLE AIV

6.7 M/S FORCE-DEFORMATION PLOTS

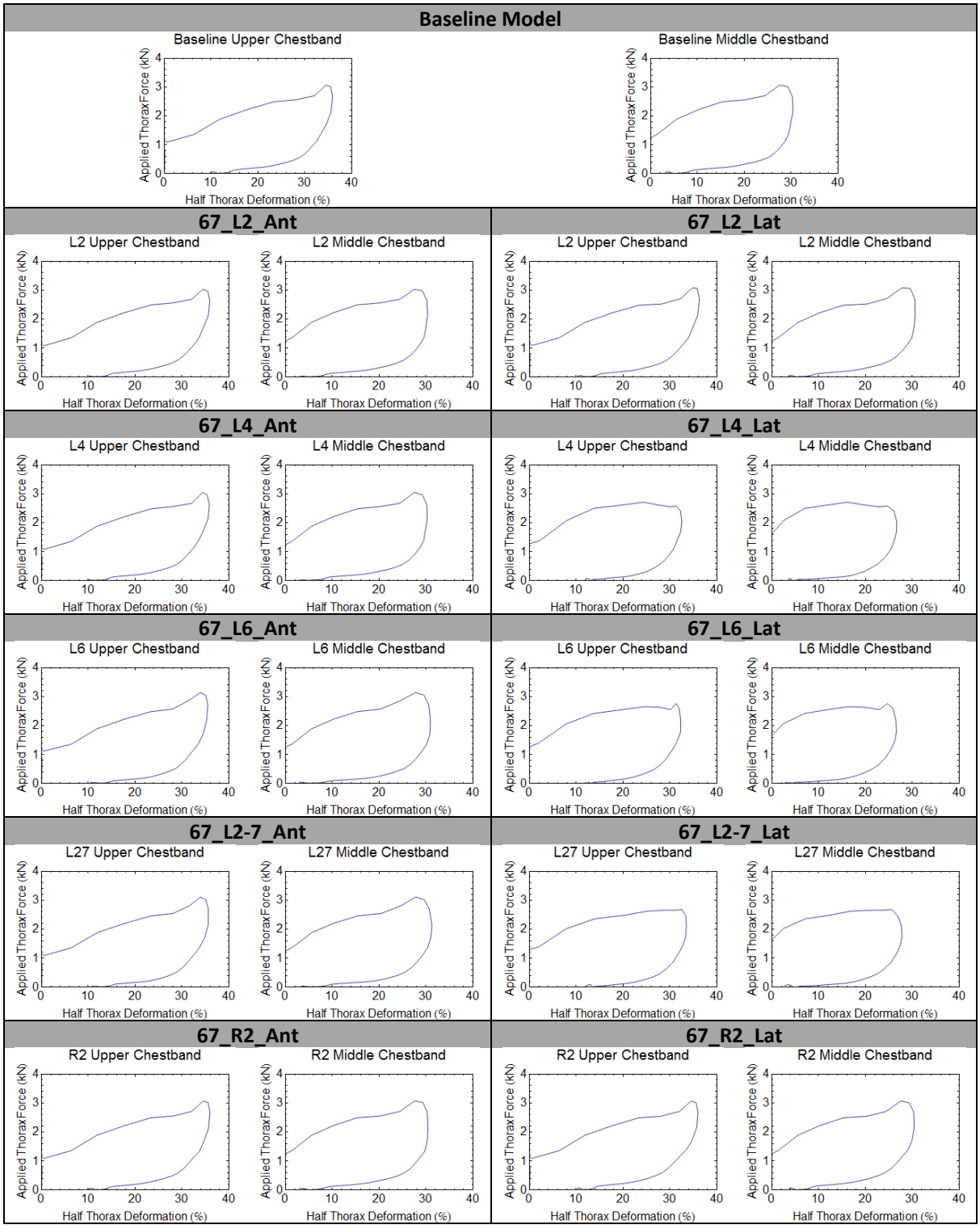

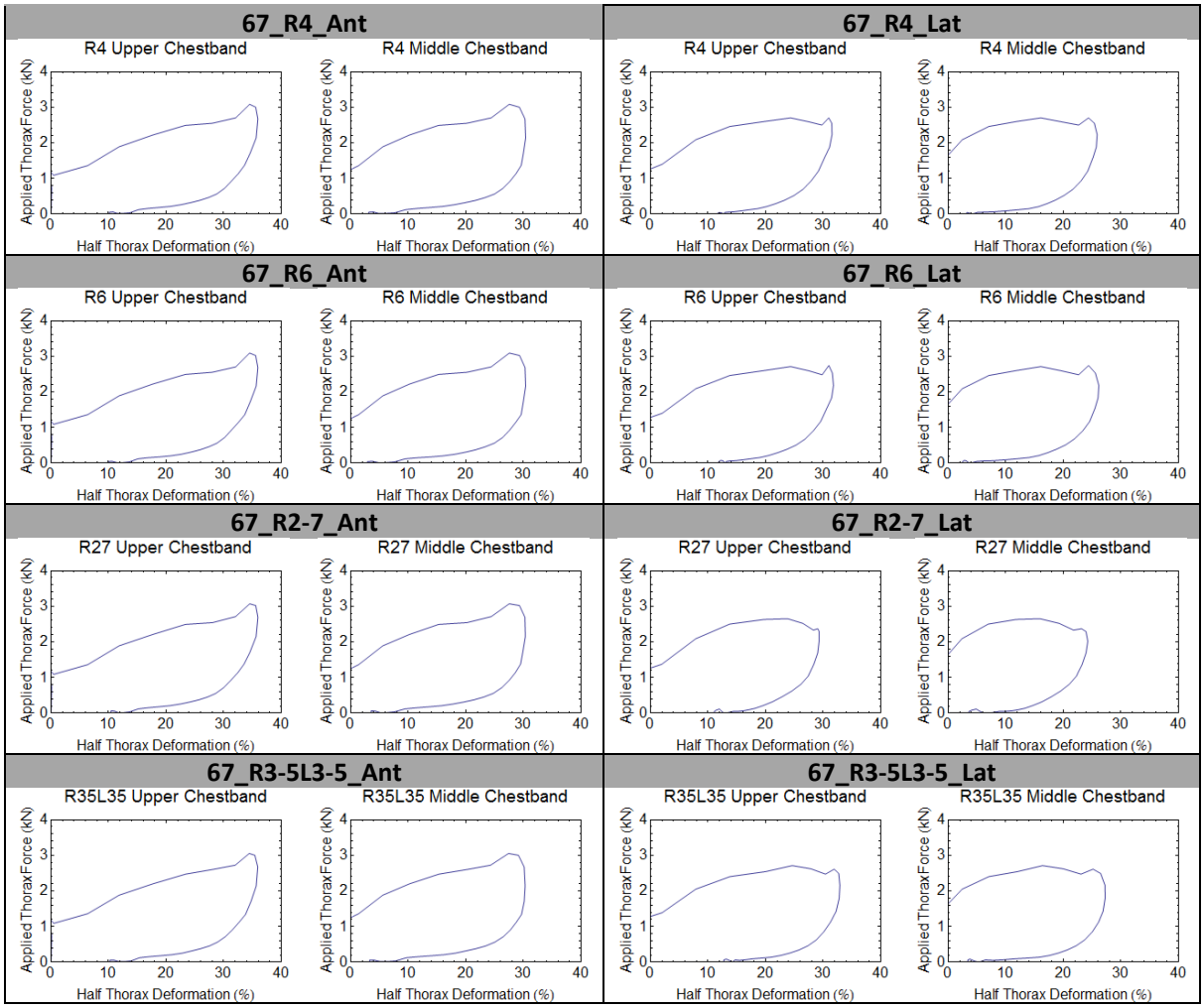
67_R4_Ant
R4 Upper Chestband
R4 Middle Chestband
67_R4_Lat
R4 Upper Chestband
R4 Middle Chestband
67_R6_Ant
R6 Upper Chestband
R6 Middle Chestband
67_R6_Lat
R6 Upper Chestband
R6 Middle Chestband
67_R2-7_Ant
R27 Upper Chestband
R27 Middle Chestband
67_R2-7_Lat
R27 Upper Chestband
R27 Middle Chestband
67_R3-5L3-5_Ant
R35L35 Upper Chestband
R35L35 Middle Chestband
67_R3-5L3-5_Lat
R35L35 Upper Chestband
R35L35 Middle Chestband
Applied ThoraxForce (kN)
Half Thorax Deformation (%)

TABLE AV

8.9 M/S FORCE-DEFORMATION PLOTS

Baseline Model

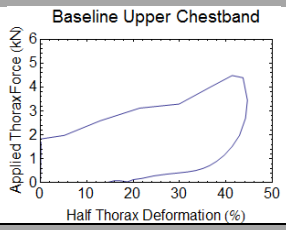

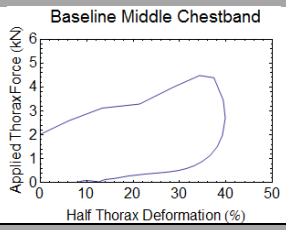

89_L2_Ant

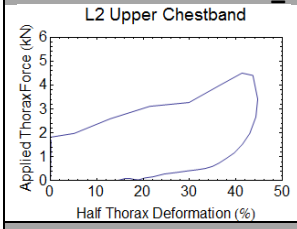

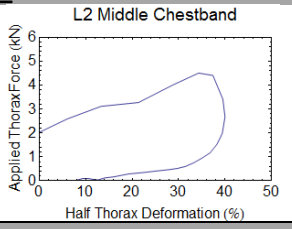

89_L2_Lat

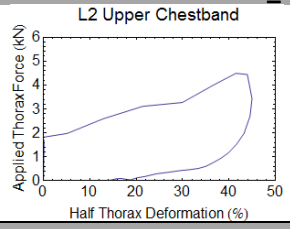

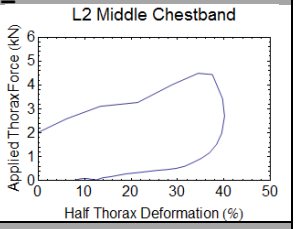

89_L4_Ant

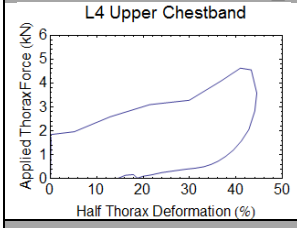

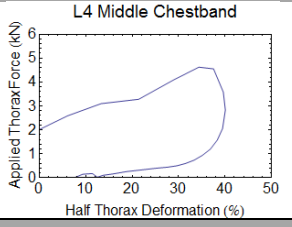

89_L4_Lat

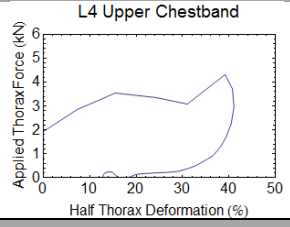

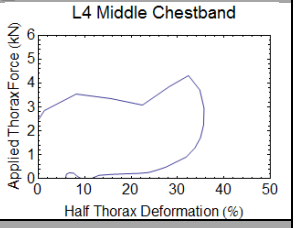

89_L6_Ant

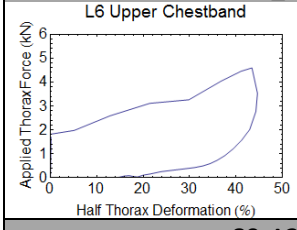

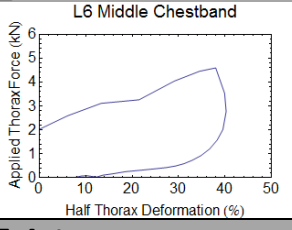

89_L6_Lat

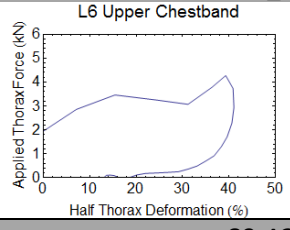

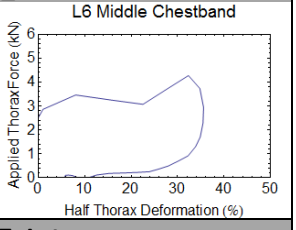

89_L2-7_Ant

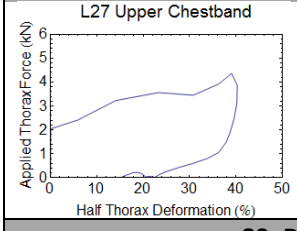

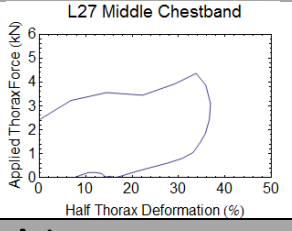

89_L2-7_Lat

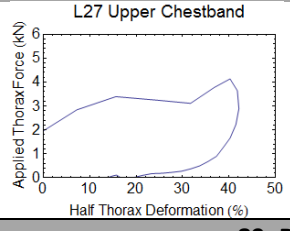

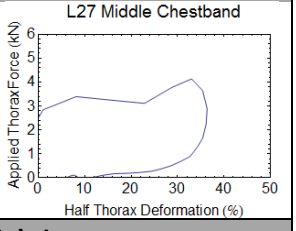

89_R2_Ant

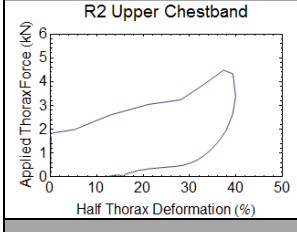

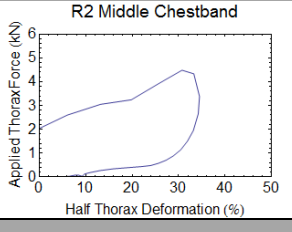

89_R2_Lat

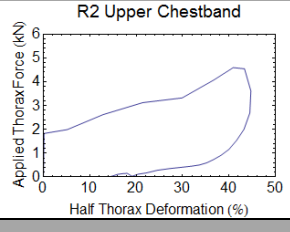

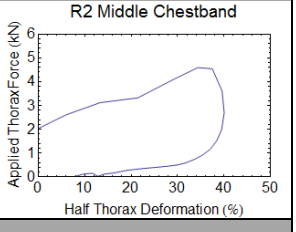

89_R4_Ant

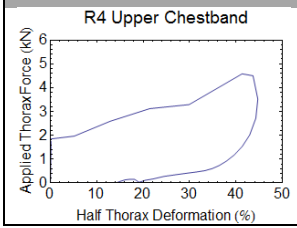

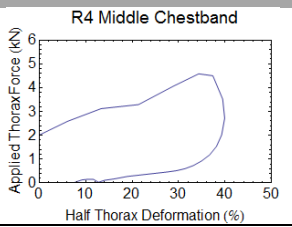

89_R4_Lat

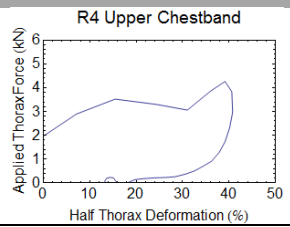

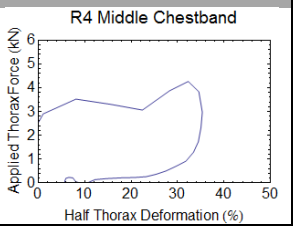

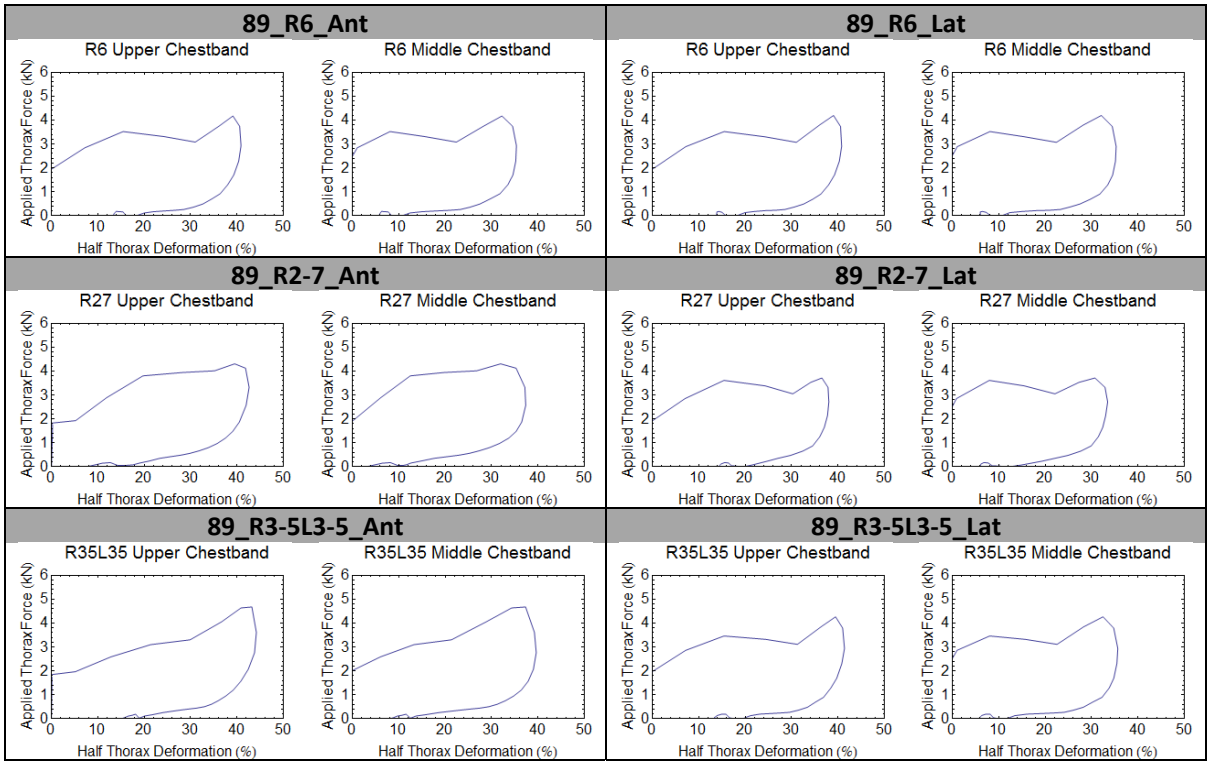
89_R6_Ant
R6 Upper Chestband
R6 Middle Chestband
89_R6_Lat
R6 Upper Chestband
R6 Middle Chestband
89_R2-7_Ant
R27 Upper Chestband
R27 Middle Chestband
89_R2-7_Lat
R27 Upper Chestband
R27 Middle Chestband
89_R3-5L3-5_Ant
R35L35 Upper Chestband
R35L35 Middle Chestband
89_R3-5L3-5_Lat
R35L35 Upper Chestband
R35L35 Middle Chestband
Applied ThoraxForce (kN)
Half Thorax Deformation (%)